Materials Chemistry and Physics 341 (2025) 130885

Contents lists available at ScienceDirect

Materials Chemistry and Physics

journal homepage: www.elsevier.com/locate/matchemphys

Fabrication of Ag/SiO_2 nanocomposite via the Stöber and chemical reduction approach for detecting sub-ppm tetracycline concentration

Nguyen Thi Hue [a], Tien Dai Nguyen [b,c,*], Hong Van Bui [d,**], Thi Bich Vu [b,c,***], Dang Van Thai [b], Thuy Phuong Nhat Tran [b], Duc Tran Trong [d], Huong Giang Nguyen Thi [d], Quoc Tran Ha [d], Nguyen Manh Hung [e]

[a] Hung Vuong University, Viet Tri City, Phu Tho 35000, Viet Nam
[b] Institute of Theoretical and Applied Research, Duy Tan University, Hanoi, 100000, Viet Nam
[c] Faculty of Natural Sciences, Duy Tan University, Da Nang, 550000, Viet Nam
[d] VNU University of Science, Vietnam National University-Hanoi, Hanoi 100000, Viet Nam
[e] Department of Materials Science and Engineering, Le Quy Don Technical University, 236 Hoang Quoc Viet, Hanoi 100000, Viet Nam

HIGHLIGHTS

- Ag NPs decorated SiO_2 NS was synthesized via the Stöber and chemical reduction method.
- Uniform SiO_2 NSs and Ag NPs with diameter sizes of 200 nm and 9.8 nm, respectively were obtained.
- Ag/SiO_2 showed enhanced surface plasmon resonance property and enhanced factors of 10^6 for the SERS substrate.
- The Ag/SiO_2 nanocomposite as SERS substrate candidate for detecting 0.01 ppm tetracycline concentration application.

GRAPHICAL ABSTRACT

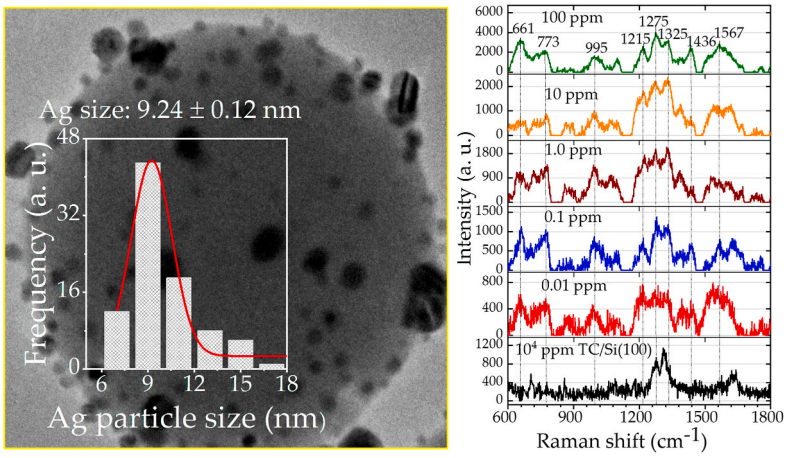

ARTICLE INFO

Keywords:
Ag/SiO_2 nanocomposite
Stöber method
SERS
Tetracycline
Antibiotic

ABSTRACT

In this work, we report the synthesis of an Ag/SiO_2 nanocomposite (NC) via the Stöber method coupled with chemical reduction for the sensitive detection of tetracycline (TC) antibiotic at sub-ppm levels. The Ag/SiO_2 NC consists of monodisperse SiO_2 nanospheres (NSs) (~200 nm) decorated with Ag nanoparticles (NPs) of approximately 9.8 nm. Structural analysis confirms that the Ag NPs exhibit a highly pure face-centered cubic (*FCC*) phase with well-defined crystallinity. The Ag/SiO_2 NC demonstrates strong surface plasmon resonance

* Corresponding author. Institute of Theoretical and Applied Research, Duy Tan University, Hanoi, 100000, Viet Nam.
** Corresponding author. VNU University of Science, Vietnam National University-Hanoi, Hanoi 100000, Viet Nam.
*** Corresponding author. Institute of Theoretical and Applied Research, Duy Tan University, Hanoi 100000, Viet Nam.
E-mail addresses: nguyentiendai@duytan.edu.vn (T.D. Nguyen), buihongvan@hus.edu.vn (H.V. Bui), vuthibich@duytan.edu.vn (T.B. Vu).

https://doi.org/10.1016/j.matchemphys.2025.130885
Received 12 November 2024; Received in revised form 12 April 2025; Accepted 15 April 2025
Available online 17 April 2025

(SPR) effects, with a characteristic peak at 400 nm, attributed to the interaction between the Ag NPs and the surface of SiO_2, thereby enhancing surface-enhanced Raman scattering (SERS) response. Leveraging these properties, we fabricated a SERS-based sensor using the Ag/SiO_2 NC for TC detection at room temperature (RT), achieving high sensitivity, selectivity, and rapid response within a concentration range of 0.01–1.0 ppm. These findings underscore the potential of Ag/SiO_2 NCs as advanced materials for chemical sensing applications, benefiting from enhanced SPR effects, superior light trapping, and increased Raman signal amplification, thereby significantly improving the detection limit.

1. Introduction

Antibiotics have long attracted significant attention in medicine, healthcare, and life science due to their critical role in treating bacterial and viral infections in humans, animals, and plants [1–5]. Among them, TC is a widely used broad-spectrum antibiotic, particularly in livestock, due to its cost-effectiveness and broad utility in preventing infections [3,6–9]. Structurally, TC is a complex molecule comprising four interconnected rings, including A (1–2–3–4–4a–12a–1), B (4a–5–5a–11a–12a–4a), C (5a–6–6a–10a–11–11a–5a), and D (6a–7–8–9–10–10a–6a) rings, and hydrophilic functional groups (e.g. –OH, O═C–NH, C═H, –(N–H)CH_3)$_2$), which contribute to its solubility in water, acidic, and alkaline solutions [10–12]. TC is part of a broader class of antibiotics that includes oxytetracycline ($C_{22}H_{24}N_2O_9$- OTC) and chlortetracycline ($C_{22}H_{23}ClN_2O_8$-CTC), each characterized by slight molecular variations that influence their pharmacokinetics and pharmacodynamics.

The widespread use of TC raises concerns about its persistence in biological systems and the environment, as up to 70 % of administered TC can be absorbed through various pathways, including the digestive system, tissues, body fluids, and even maternal transmission via milk or the placenta. This extensive absorption poses potential health risks, especially with excessive TC exposure, which has been linked to adverse effects such as impaired bone development, dental discoloration, liver toxicity, digestive disorders, and the proliferation of antibiotic-resistant bacteria in the gut [13]. Therefore, regulatory standards such as Codex Alimentarius have established strict limits on TC residue in food products, with maximum allowable concentrations as low as 0.1–0.2 ppm in milk and other consumables [13]. Consequently, developing sensitive, accurate, and efficient methods for detecting TC residues in food is crucial. Various detection techniques have been employed for this purpose [14], including high-performance liquid chromatography (HPLC) [15], liquid chromatography coupled with mass spectrometry (LC-MS) [4,5], fluorescence-based assays [16–19], luminescence resonance [8], electrochemical sensors [20], enzyme-linked immunosorbent assay (ELISA) [21]. However, the HPLC, LC-MS, and ELISA techniques often suffer from limitations, such as complex sample preparation, requiring trained operators, making them time-consuming labeling steps and less accessible, limited durability, leading to false positives or inaccurate quantification, and poor suitability for rapid, on-site testing [4,5,16–19,21]. The HPLC combined with LC-MS methods-based detection has shown high accuracy. However, it is still expensive and time-consuming [22,23].

SERS has emerged as a promising alternative for detecting ultra-low concentrations of target molecules due to its simplicity, cost-effectiveness, eco-friendliness, and exceptional sensitivity [1–3,6,24,25]. SERS significantly enhances Raman sensitivity, making it a promising tool for trace detection of food contaminants such as antibiotics and pesticide residues. Advances in laser, optics, and electronics have led to portable Raman devices, improving accessibility and highlighting Raman spectroscopy's strengths in elemental chemical identification. Unlike the fluorescence resonance-based detection methods that rely on high-energy excitation, SERS utilizes low-energy/or near-infrared excitation (785 nm), which minimizes photochemical degradation of antibiotics and ensures more stable, non-destructive detection. Nowadays, SERS exploits the SPR of metallic nanoparticles to amplify Raman signals, enabling both qualitative and quantitative detection of analytes at concentrations as low as 10^{-12} to 10^{-14} M [1,2,24]. By incorporating metal NPs onto a semiconductor substrate, the Raman signal is significantly enhanced, making SERS a powerful tool for detecting trace levels of antibiotics, including TC [2,4,24,25].

Metal NPs used for SERS substrate must exhibit rapid response times, high sensitivity, and selectivity and provide more precise information than other detection methods. These advantages arise from the localized SPR of metal NPs, which amplifies the electromagnetic (EM) field and thus enhances analyte detection [1,4,24,26–35]. Besides the smaller size of nanoparticles, which increases the specific surface area, large pores improve the adsorbed capacity of organic compounds and antibiotic molecules on the surface for degradation and detection [26,36–38]. When combined with laser-based Raman spectroscopy, SERS enables qualitative or semi-quantitative analysis through superior light trapping, enhanced light scattering, and resonant cavity effects. SERS is less susceptible to photobleaching than fluorescence spectroscopy, allowing for prolonged data collection and improved reliability [1]. These advantages have led to widespread applications of SERS in food science [4,24,26,27], biomedicine [1,30], disease treatment [31,32], diagnostics [32], environmental monitoring [33,34], chemistry [28,29], optoelectronic devices [35], spectroscopy [37], and other areas [39].

Choosing metallic nanoparticles for SERS substrates is critical for optimizing sensitivity, selectivity, and signal enhancement. Noble metals such as Au, Pt [40], and Ag [41] have shown particular promise when combined with semiconductors like TiO_2, Cu_2O, SiO_2, and C_3N_4 [1,25,30,31,33,35,37,42–49]. Among them, Ag NPs deposited on SiO_2 nanostructure have demonstrated superior SERS performance due to their high surface-to-volume ratio, biocompatibility, ease of functionalization [2], and the formation of EM "hot spots" [34,50,51]. These hot spots in the gaps between closely spaced Ag NPs lead to an intense localized EM field that enhances the Raman signal.

Ag/SiO_2 nanostructures have been synthesized by various techniques, including co-precipitation [52], sol-gel [45,53], Stöber [37,44], wet impregnation [54], solvothermal [55], hydrothermal [56], sputtering [57], and atomic laser deposition [58] methods. Among these, the Stöber method, combined with chemical reduction, is particularly advantageous due to its low cost, eco-friendliness, simplicity, and ability to detect molecules at ultra-diluted concentrations. By leveraging the localized SPR effect of Ag NPs anchored on the SiO_2, these Ag/SiO_2 NCs can significantly improve the TC detection at ultra-low concentrations (10^{-10} to 10^{-14} M) via SERS. The heterostructure formed at the interface between Ag NPs and SiO_2 nanosphere promotes efficient charge transfer (CT), further enhances analyte polarization, and amplifies the Raman signal [2,59].

In this work, we present the synthesis of Ag/SiO_2 NCs via a combination of the Stöber method and chemical reduction, aiming to achieve a well-dispersed plasmonic nanostructure. Furthermore, the resulting Ag/SiO_2 NC was systematically characterized. It demonstrated promising performance as a SERS-active substrate for detecting TC at sub-ppm concentrations. These findings highlight the potential of Ag/SiO_2 NCs as a sensitive, selective, and rapid sensing platform for trace-level antibiotic detection, paving the way for developing advanced SERS-based chemical sensors.

2. Experimental procedure

2.1. Materials

Silver nitrate ($AgNO_3$, 99.99 %), tetraethoxysilane (TEOS, $Si(OC_2H_5)_4$, 99.98 %), sodium borohydride powder ($NaBH_4$, 98 %), (3-aminopropyl) trimethoxysilane (APTMS, $H_2N(CH_2)_3Si(OCH_3)_3$, 99.96 %), ammoniac (NH_3, wt. 25 %), acetone (CH_3COCH_3, 99.5 %), ethanol (C_2H_5OH, 99.5 %), hydrofluoric acid (HF, 99.99 %), and nitric acid (HNO_3, 99.999 %) were purchased from Merck. Tetracycline antibiotic was obtained from the National Institute of Drug Quality Control, Ministry of Health, Vietnam. A double-side polished and undoped Si (100) wafer (2-inch diameter, 350 μm thickness, thermal expansion coefficient (α) = 2.5 μm/m.K, and resistivity (ρ) = 5000 Ω cm) was supplied by AXT, Inc. All reagents were of high purity and used as received without further purification.

2.2. Synthesis of Ag/SiO_2 NC and SERS substrate

2.2.1. Synthesis of SiO_2 NSs

SiO_2 NSs were synthesized via a modified sol-gel method to ensure uniform size distribution and high purity. Initially, 10 mL of $Si(OC_2H_5)_4$ was dissolved in a controlled mixture of 30 mL C_2H_5OH and deionized (DI) water at a 1:1 vol ratio. The solution underwent ultrasonication for 15 min at RT to enhance hydrolysis and dispersion. Subsequently, 3 mL of NH_3 solution was introduced, and the reaction was allowed to proceed under continuous stirring for 4 h to promote the condensation of SiO_2 precursors. The resulting SiO_2 NSs were isolated by centrifugation, thoroughly washed with C_2H_5OH and DI water to remove residual reactants, and dried at 80 °C for 15 h to obtain a highly stable SiO_2 powder.

2.2.2. Synthesis of Ag/SiO_2 NC

The Ag/SiO_2 NCs were synthesized via a controlled reduction process to achieve homogeneous Ag NPs deposition on the SiO_2 NS surface. Initially, 0.18 g of $AgNO_3$ was dissolved in 10 mL of DI water. Then, 3 mL of NH_3 was added under magnetic stirring for 10 min to form a stable silver-ammonia complex (solution #1). Concurrently, 0.01 g of $NaBH_4$ was dissolved in 10 mL of DI water and stirred for 10 min to prepare the reducing agent solution (solution #2). To deposit Ag NPs on the SiO_2 NS surface, the SiO_2 NS was functionalized using APTMS. Specifically, 0.2 g of SiO_2 powder was ultrasonicated in 50 mL of C_2H_5OH for 15 min at RT (solution #3) to ensure uniform dispersion. Subsequently, 0.01 g of APTMS was introduced into solution #3 and stirred for 15 h to modify the SiO_2 NS surface with amine groups chemically, enhancing Ag NP adhesion. The functionalized SiO_2 (APTMS-SiO_2) was collected via centrifugation at 3500 rpm for 10 min. The deposition of Ag NPs onto SiO_2 was achieved by dispersing the APTMS-SiO_2 in solution #1 and stirring for 2 h to promote Ag^+ ion adsorption (solution #4). Finally, solution #2 was gradually introduced into solution #4, triggering the reduction of Ag^+ ions and the subsequent formation of the Ag NPs on the SiO_2 NS surface. The reaction was maintained for 15 min to ensure a complete Ag/SiO_2 NC precipitate. The resulting Ag/SiO_2 NC was collected, washed extensively with DI water and C_2H_5OH to remove excess reactants, and dried at 80 °C for 15 h. The detailed formation and mechanism of the Ag/SiO_2 NC can be referred to in *Refs.* [37,60] and Fig. 1.

2.2.3. Fabrication of the SERS substrate

A double-side polished Si(100) wafer (1.0 cm × 1.0 cm) was ultrasonically cleaned in acetone, ethanol, and DI water three times for 15 min. To remove the native SiO_2 layer, the wafer was immersed in 50 % HNO_3 and 6 % HF for 15 min, then rinsed thoroughly with DI water several times and dried under N_2 gas at 50 °C for 1 h. Afterward, 0.1 g of Ag/SiO_2 NC was dissolved in 10 mL of DI water and stirred for 5 min. A 10 μL aliquot was drop-cast onto the Si(100) surface three times, allowing each layer to dry naturally at RT to ensure uniform coverage. Subsequently, to evaluate SERS performance, 10 μL of a 100 ppm TC solution was deposited onto the Ag/SiO_2/Si(100) substrate, covering a 12.56 mm^2 area, and dried at RT. The same procedure was applied for

Table 1
Parameters for the preparation of SERS substrate using Ag/SiO_2 NC and varying TC concentrations.

Synthesis & deposition method	$AgNO_3$	SiO_2 pow.	TC concentration	Ag/SiO_2 pow.	Si(100) sub. area
	(g)	(g)	(ppm)	(g)	mm^2
Coating	–	–	powder	–	12.56
Coating	–	–	10^4	–	12.56
Chemical reduction & Stöber	0.18	0.2	–	0.01	–
Coating	0.18	0.2	0.01 ÷ 100 (increment 10)	0.01	12.56

– non-investigation; pow. – powder; sub.– substrate.

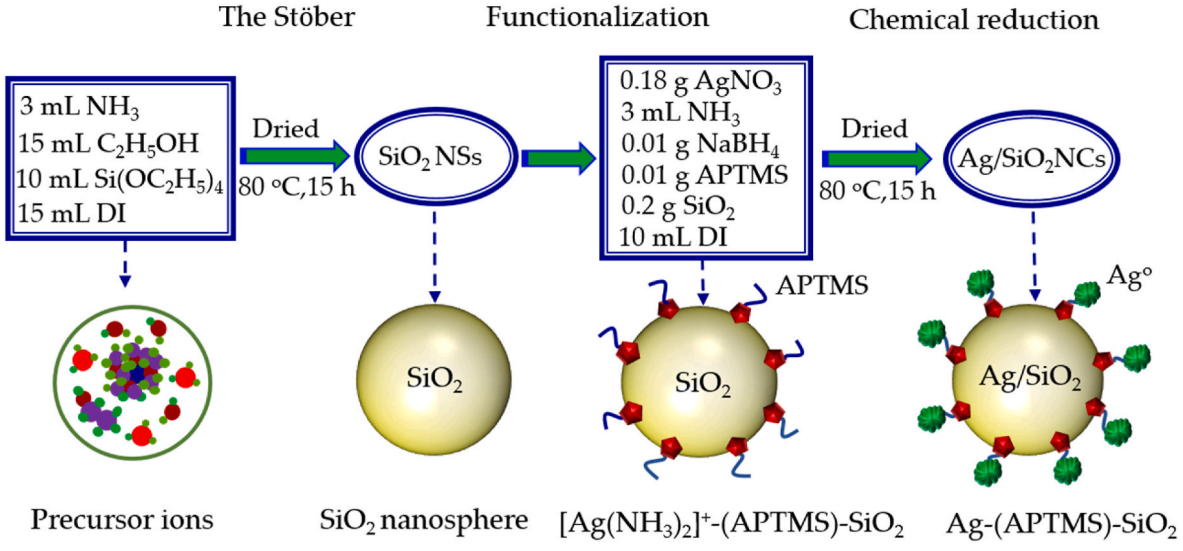

Fig. 1. Schematic synthesis process of the Ag/SiO_2 NC.

TC solutions of varying concentrations (0.01–100 ppm) to assess detection sensitivity (as listed in Table 1). Further details of this procedure can be referred to the previous report [37].

2.3. Material characterizations and TC sensor performance evaluation

The microstructural morphology of the Ag/SiO_2 NCs was characterized by high-resolution transmission electron microscopy (HR-TEM, JEM-2100, Japan). The surface area characteristic of the material was investigated by the Brunauer Emmett and Teller technique (BET, Micromeritics, TriStar II 3020 3.02). The analysis of surface atom electronic structure and chemical composition of the Ag/SiO_2 NC was performed by X-ray photoelectron spectroscopy (XPS, Thermo Fisher Scientific, NX10). The crystalline structure of the Ag/SiO_2 NCs was investigated by X-ray diffraction technique (XRD, PANalytical Empyrean, Cu_K_α radiation, $\lambda = 1.54056$ Å). The optical properties of the samples were analyzed using UV–Vis (UV-2450), and Fourier-transform infrared (FT-IR-6300, Jasco) spectroscopy, with data collected in the wavelength range of 200–700 nm and the wavenumber range of 500–4000 cm^{-1}. Raman spectroscopy (μRaman-Ci, Technospex, 10 mW, excitation wavelength of 785 nm) was employed to evaluate the SERS properties of the materials. Further details on the equipment's information, setup, and operation can be found in Refs. [37,60].

3. Results and discussion

Fig. 2 shows the TEM images of the Ag/SiO_2 NC, illustrating the morphology of the NSs with attached Ag NPs. As shown in Fig. 2(a), the Ag NPs and SiO_2 NSs were successfully co-synthesized via the Stöber method combined with chemical reduction. The SiO_2 NSs exhibit a rough surface, decorated with uniformly dispersed Ag NPs, as observed in Fig. 2(b). The TEM analysis revealed that the Ag NPs range in size from 6 to 18 nm, with a predominant average diameter of 9.24 ± 0.12 nm (inset of Fig. 2(b)). The as-synthesized SiO_2 NSs are uniformly spherical with an average diameter of approximately 200 nm, consistent with previous reports [37]. Fig. 2(c) displays the HR-TEM image showing clear lattice fringes of the Ag NPs, though the SiO_2 NSs are not visible due to their larger diameter. The measured d-spacing of approximately 2.4 Å corresponds to the (111) plane of the Ag crystal [37]. These results confirm that the Ag NPs were successfully synthesized on the surface of the SiO_2 NSs with uniform size and high crystalline quality. The size of the Ag NPs, which is neither too large nor too small, is ideal for enhancing the plasmonic resonance effect in the SERS substrate. This size range increases the surface area-to-volume ratio and induces a quantum confinement effect, leading to an expansion of the light absorption region. Additionally, it accelerates CT to promote analyte polarization, enhances short-range chemical interactions, improves Raman signal amplification, and provides superior electronic conductivity [2]. The BET analysis Ag/SiO_2 NC gives an average surface area of 10.8946 ± 0.1072 $m^2\ g^{-1}$ and Langmuir surface area of 20.9393 ± 0.6994 $m^2\ g^{-1}$, adsorption pore width of 11.0704 nm, as seen in Fig. S1 of the Supporting Information. The result might be evaluated in the Ag/SiO_2 NC sized around 200 nm, suggesting a mesoporous structure [61].

Fig. 3 shows the XRD pattern of the as-synthesized nanospherical SiO_2 and Ag/SiO_2 NC, confirming the presence of Ag NPs and their crystalline quality. In Fig. 3(a), the diffraction peaks at 2θ of 38.1°, 44.3°, and 64.4° correspond to the (111), (200), and (220) planes of the *FCC* structure of the Ag (*JCPDS No. 04*–0783) [24,45,50,62–66], which belongs to $Fm\bar{3}m$ space group.

A weak and broad peak at 2θ of 23.9° is assigned to the (100) plane of SiO_2 [37,67], indicating the amorphous nature of the SiO_2 structure. In contrast, the sharp and intense peak at 2θ = 38.1°, corresponding to the (111) plane, signifies the high crystallinity of the Ag NPs, with a photograph inset of Ag/SiO_2 NC on Si(100) substrate, as shown in Fig. 3 (b). This plane indicates that the Ag nanocrystals predominantly exhibit the (111) orientation, with well-defined and distinct phases. The average crystallite size and d-spacing of the Ag NPs were calculated to be approximately 9.80 and 0.24 nm, respectively. These values were estimated using Debye-Scherrer's equation (1) and Bragg's law (2) below:

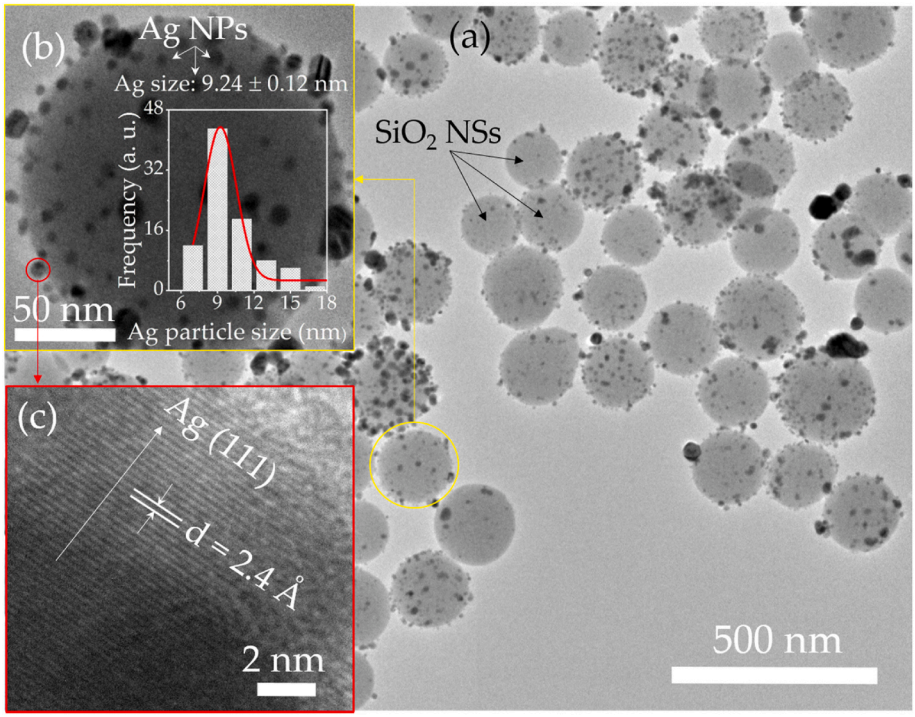

Fig. 2. (a) (Color online) TEM image of Ag/SiO_2 NCs; (b) Magnified view of Ag NPs on SiO_2 NSs, with an inset showing the size distribution histogram of Ag NPs on the SiO_2 surface; and (c) HR-TEM image of Ag NPs. (For interpretation of the references to color in this figure legend, the reader is referred to the Web version of this article.)

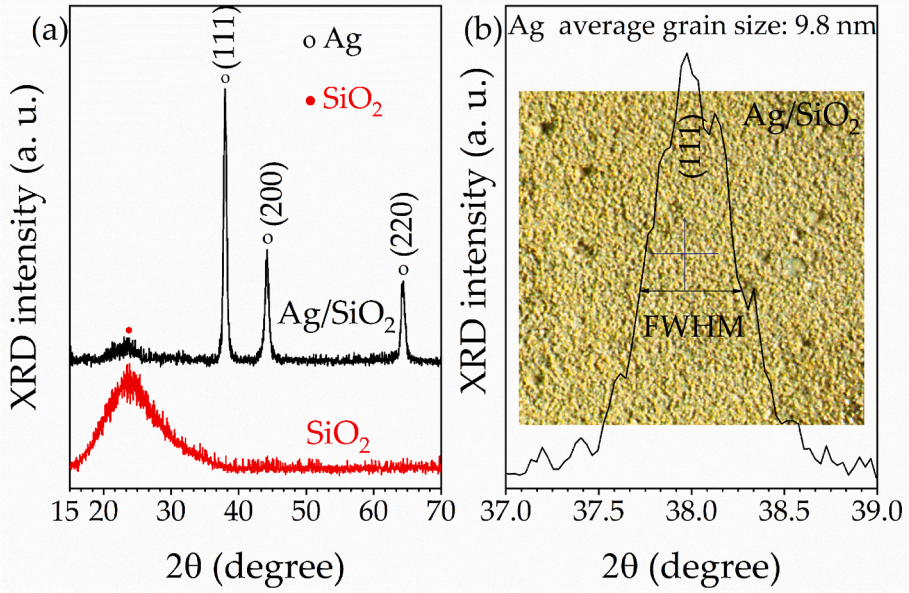

Fig. 3. (a) (Color online) XRD patterns of SiO_2 NSs and Ag/SiO_2 NC; and (b) Magnified view of (111) plane of Ag NPs for evaluating Ag grain size with inset photograph of a macroscopic digital of Ag/SiO_2 NC on Si(100) substrate. (For interpretation of the references to color in this figure legend, the reader is referred to the Web version of this article.)

$$D_{aver.} = \frac{0.9\lambda}{\beta \cos\theta}, \quad (1)$$

$$2d \sin\theta = n\lambda, \quad (2)$$

where $D_{aver.}$ is the average size of the crystallite (nm), λ is the wavelength of X-ray (0.15406 nm), θ is Bragg's diffraction (radian), and β is the full-width half maximum (FWHM) of the diffraction peak (radian). The XRD-derived crystallite size and d-spacing are in close agreement with the TEM result for the Ag/SiO_2 NC, confirming the formation of pure, well-crystallized Ag NPs on the SiO_2 NSs with no detectable impurities.

Fig. 4(a) shows the FT-IR spectra of the SiO_2 NSs and Ag/SiO_2 NC, measured at RT. The Ag/SiO_2 NCs sample exhibits eight absorption peaks at 471, 554, 803, 976, 1100, 1639, 1872, and 3420 cm^{-1}, ranging from 400 to 4000 cm^{-1}. Specifically, the absorption peaks at 471 δ(Si–O–Si), 803 υ_s (Si–O–Si), and 1100 cm^{-1} υ_{as} (Si–O–Si) correspond to the out-of-plane bending and stretching vibration of Si–O bonds [64, 68–70]. The prominent peak at 1100 cm^{-1} indicates the formation of a well-defined and stoichiometric SiO_2 structure. Additionally, the peak at 976 cm^{-1} δ(Si–O–H) is attributed to Si–OH bending vibration [64,67]. The absorption bands at 1639, 1872, and 3420 cm^{-1} correspond to C═O stretching, C═O bending, and O–H stretching vibration, respectively, indicating the presence of residual functional groups on the surface of the Ag/SiO_2 NSs. Many OH, H–O–H, and Si–OH groups are present on the surface of SiO_2, which serve a key role in bonding the Ag ion from the

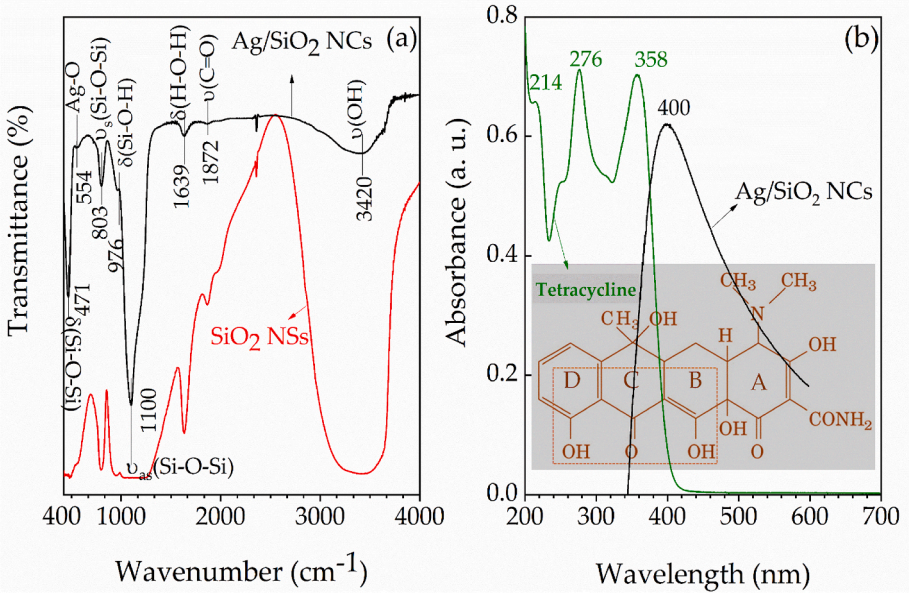

Fig. 4. (a) (Color online) FT-IR spectra of SiO_2 NSs and Ag/SiO_2 NC; and (b) UV–Vis spectra of Ag/SiO_2 NCs and commercial tetracycline antibiotic with inset photograph of tetracycline antibiotic structure. (For interpretation of the references to color in this figure legend, the reader is referred to the Web version of this article.)

sol to form Ag/SiO_2 NC [69]. The large amount of water with the O–H group on the surface could be decreased via heating. Notably, the weak absorption peak at 554 cm^{-1} is associated with the Ag–O stretching vibration of Ag_2O [32,53,71], confirming the presence of Ag NPs on the SiO_2 NSs.

The vibrational modes observed at 803, 976, and 1100 cm^{-1} in the Ag/SiO_2 NCs shift to higher wavenumbers and increase intensity than those in the SiO_2 NSs. This shift is attributed to the increased vibrational energy and the enhancement of the silica network structure. Additionally, the Si–OH peak shift at 976 cm^{-1} towards higher wavenumbers is likely due to an increased force constant of the Si–OH bonds, originating from water adsorption on the SiO_2 surface. This effect can be minimized by annealing or storing the sample under vacuum conditions [64,72].

Fig. 4(b) displays the UV–Vis absorption spectra of the Ag/SiO_2 NC and commercial TC antibiotic measured at RT. The Ag/SiO_2 NC shows a strong absorption peak at 400 nm due to the Mei plasmon resonance excitation from the Ag NPs on the surface of the SiO_2 [24,37,50,64,73]. This absorption peak suggests that the Ag NPs are quasi-spherical in shape with a well-concentrated size distribution [37,45,74], corroborating the TEM-derived particle sizes shown in Fig. 2(b). Additionally, Fig. 4(b) includes the UV–Vis spectrum of a commercial TC solution in DI water. The spectrum shows absorption peaks at 276 and 358 nm, corresponding to the A ring chromophore (CO1, amide, and CH_3 groups) and the BCD ring chromophore, respectively [15,75–78]. The absorption peak at 276 nm results from a π−π* transition within the tricarbonyl system of the A ring. In comparison, the band at 358 nm relates to the π−π* transition within the BCD chromophore [77,78]. The absorption peak at 358 nm in the visible range determines TC concentration [79,80]. In addition, a weaker peak at 214 nm is associated with the π−π* transition within the BCD ring chromophore, related to the D ring phenyl group of the β-hydroxy ketone system. This transition is linked to deprotonation processes that occur at low pH (<7.0), indicating sensitivity to deprotonation and metal coordination effects [77,78].

Fig. 5 presents the representative survey and high-resolution XPS spectra of the Ag/SiO_2 NC. The survey spectra confirm the presence of Si, O, and Ag elements, and no other elements are detected except for the C element, as seen in Fig. 5(a). The XPS of the Si 2p spectrum showed two decomposed peaks corresponding to the Si–O–Si bond (102.23 eV) and the Si–O bond (at 103.32 eV), which are attributed to SiO_2 and Si–O–Si links between APTMS-bonded molecules [38], as shown in Fig. 5(b). The XPS spectrum of the O 1s profile indicated four decomposed peaks at 530.8 eV, 531.4 eV, 532.2 eV, and 533.4 eV, corresponding to the elements of Ag–O, –OH, -Si-O-Si-, and -Si-O, as shown in Fig. 5(c). This indicates the presence of APTMS on the SiO_2 NSs, besides the FT-IR spectra (Fig. 4(a)). Note that the XPS of Ag 3d exhibits two peaks at binding energies of 368.9 eV and 374.9 eV, corresponding to Ag $3d_{5/2}$ and Ag $3d_{3/2}$, respectively.

The spin splitting of the 3d doublet of Ag is 6.0 eV, confirming the presence of Ag NPs and the Ag^0 state. The high-resolution Ag 3d spectrum was decomposed by four peaks at binding energies of (368.9; 375.1 eV) and (367.8; 373.7 eV), indicating the appearance of small proportions of Ag and Ag–O along with metallic Ag NPs [81]. The elemental compositions were extracted using XPS data, which were 61.18 % at. of O, 32.44 % at. of Si, and 6.38 % at. of Ag. The results differed from the EDX analysis, as seen in Fig. S2 of the Supporting Information. Because it only indicates the elemental compositions of the $AgSiO_2$ compound, the composite primarily includes O, Si, and Ag. There is a blueshift in the binding energies of Ag 3d peaks compared to the theoretical calculation (368.2, 374.2 eV), attributed to a depletion of the electron density of Ag atoms. Regarding Ag/SiO_2 NC, Ag atom tends to lose electrons primarily due to chemical interactions between functional groups (-OH, –C═O) of APTMS and the surface of SiO_2 [82,83]. The electronegativity difference between Ag (1.94) and O (3.44) [84], combined with nanoscale surface effects [85], facilitates electron withdrawal from Ag atoms, resulting in a decrease in electron density. This mechanism manifests as a partial oxidation state of the silver

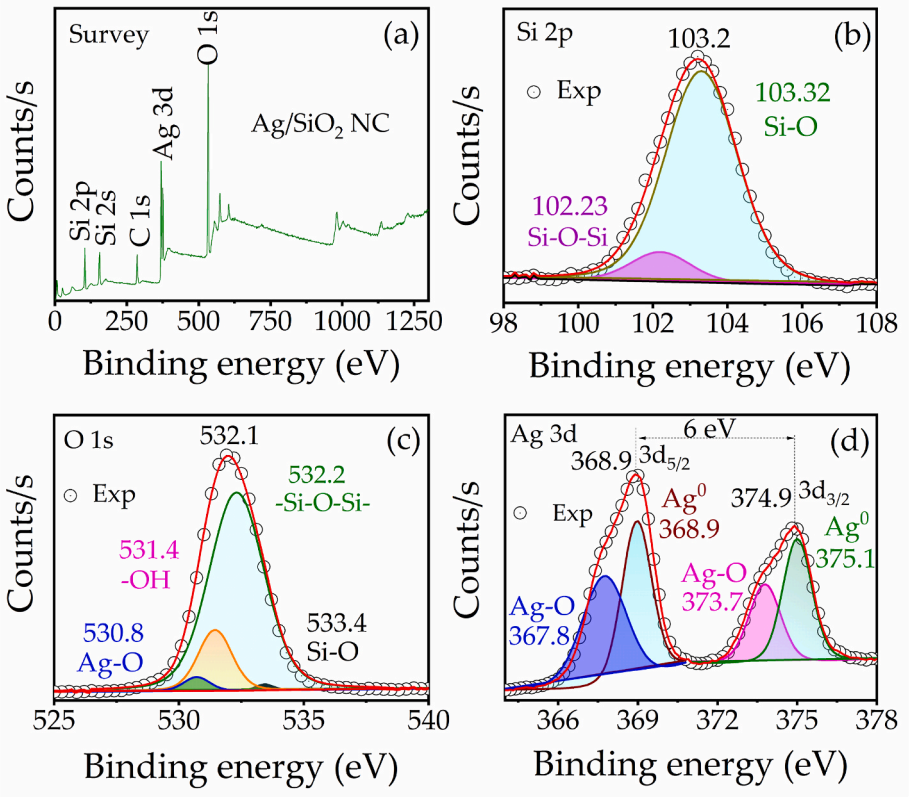

Fig. 5. (a) (Color online) The XPS survey spectrum; High-resolution spectra of (b) Si 2p electrons of silica, (c) O 1s electrons of oxygen, and (d) Ag 3d electrons of silver of Ag/SiO_2 NC. (For interpretation of the references to color in this figure legend, the reader is referred to the Web version of this article.)

element to form an Ag–O bond, which is evidenced by a positive shift in the binding energy of the Ag 3d peaks in the XPS spectrum.

Fig. 6(a) illustrates the Raman spectrum of the commercial TC powder, measured at RT using a 785 nm laser excitation source. The Raman spectrum reveals a series of distinct peaks at 579, 670, 710, 859, 949, 1060, 1140, 1174, 1292, 1315, 1449, 1563, and 1625 cm^{-1}. Among these, the vibrational modes at 1625, 1449, 1315, and 1292 cm^{-1} are particularly significant for identifying TC. Two prominent Raman peaks are observed around 1625 and 1315 cm^{-1}. The peak at 1625 cm^{-1} is assigned to a combination of vibrational modes, including ν(O–C1), ν(C2–C3), δ(amid-CO), δ(amid-NH), and other amide-related stretching and bending vibrations. The peak at 1315 cm^{-1} is assigned to ring breathing modes such as ν(C10–C10a), ν(C6a–C7), and ν(C9–C10), which are associated with the planar C9 to C12 region of the TC molecular structure.

In addition to these strong modes, medium-intensity vibrations are seen at approximately 1563, 1449, and 1292 cm^{-1}. The peak at 1563 cm^{-1} is attributed to δ(OH10,12) stretching, ν(C11aC12) bending, and ν(D) stretching of the benzene ring D. The peak at 1292 cm^{-1} is assigned to a complex set of vibrations, including δ(CH4,4a,5,5a), δ(OH12), δ(amid-NH) bending, and various stretching modes such as ν(CO10), ν(CO3), ν(CH7,8,9), ν(amid-NC), ν(C4a C5), as well as ν(D) stretching of the benzene ring D [10,86,87]. A weaker variation mode is identified at 1449 cm^{-1}, which is linked to δ(amid-CH_3) stretching, δ(CH7,8,9) bending, δ(OH12) bending, and ν(CO10, CO11, CO12) stretching, as well as ν(D) stretching of the benzene ring. The detailed assignments of these variational modes across various frequencies are listed in Table 2, and further references can be found in the literature [10,86].

Fig. 6(b) presents the SERS spectra of 100 ppm TC on both bare Si (100) and Ag/SiO_2/Si(100) SERS substrates in the 600–1800 cm^{-1} range. The Raman signal of the TC on the Ag/SiO_2/Si(100) substrate exhibits significantly higher intensities with well-defined vibrational modes. In contrast, the Raman modes of TC on the bare Si(100) substrate are weak and poorly resolved, indicating limited signal enhancement in the absence of the SERS-active substrate. Additionally, there are non-SERS spectra of the Ag/SiO_2/Si(100) substrate. Distinct Raman peaks of TC at 1564, 1446, 1325, 1275, and 1215 cm^{-1} are observed on both Si (100) and Ag/SiO_2/Si(100) SERS substrates. However, the intensities of these peaks are significantly enhanced on the SERS substrate, with more precise and more distinct vibrational features. This enhancement is attributed to the SERS effect, where combining plasmonic Ag NPs and

Table 2
Raman vibration peaks of the Tetracycline.

Raman shift positions (cm^{-1})	Description of normal modes	Vibration intensity (arb. units)
1619/1617	ν(CO1), ν(amid-CO), δ(amid-CNH), ν(CO3), ν(C2C3), ν(OH10,12),ν(amid-CO2)	Very strong
1590	δ(OH10,12), ν(D), ν(C11aC12)	Weak
1573/1560		
1480	δ(CH7,8,9), δ(OH12), ν(D), ν(CO10,CO11, CO12), δ(amid-CH_3)	
1449/1450		
1314/1311	ν(C9C10,C10C10a,C10aC11), ν(CO11,12), ν(CO3), δ(CH7,8,9)	Very strong
1278	δ(CH4, 4a, 5, 5a), δ(OH12), δ(amid-NH), ν(CO10), ν(CO3), ν(CH7,8,9), ν(amid-NC), ν(C4aC5), ν(D)	Medium
1252	δ(CH4,5a,5,5a), δ(CH10), δ(CH7,8,9), δ(OH12), ν(D)	
1249	ν(CO10)	
1183	ν(CO3)	
1170	ν(CO10)	Weak
1141/1060/ 1137	ν(CO6,12)	Medium
1060	ν(CO3)	Weak
942/947		
719	w(amin-NH), w(amin- NH_2), ν(CO6,12), γ(OH3,6,10,12,12a)	
594/597	δ(amid-ONH)	

γ – stretching; δ – bending.

SiO_2 nanostructures creates "hotspots" that interact with TC molecules, resulting in amplified Raman signals. Among these, the vibrational mode at 1275 cm^{-1} shows the most vigorous intensity (~4000 a.u.). Several additional TC vibrational modes at 597, 670, 710, 859, 949, 1060, 1140, and 1174 cm^{-1} overlap with vibrational modes from the Si and SiO_2 substrates at 624, 665, 825, 980, 1073, 1106, 1144, and 1177 cm^{-1} [12,88]. These substrate-related vibrations, primarily associated with silicon oxide [88], exhibit significantly lower intensities than the prominent TC peaks, ensuring minimal interference in TC detection. The vibration modes at 1564, 1446, 1325, 1275, and 1215 cm^{-1} are key markers for future TC identification on the SERS substrates, providing a reliable and enhanced signal. These bands were used to compare signal intensities across different substrates. To further optimize the SERS performance for TC detection at RT, the TC concentration on the

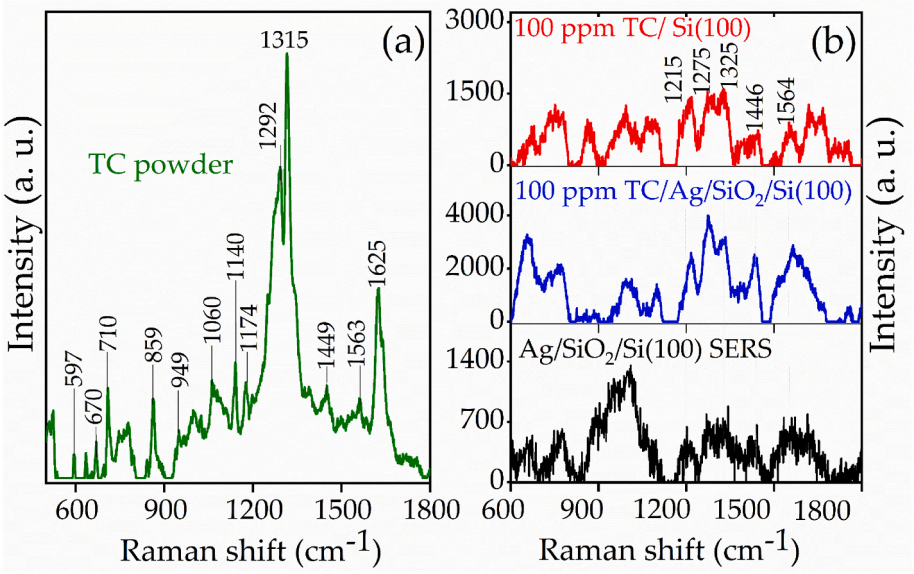

Fig. 6. (a) (Color online) Raman spectrum of commercial TC powder, and (b) SERS spectrum of 100 ppm TC on various substrates with an acquisition time of 30 s. (For interpretation of the references to color in this figure legend, the reader is referred to the Web version of this article.)

$Ag/SiO_2/Si(100)$ SERS substrate was systematically varied, allowing the determination of the lowest detectable concentration under these conditions.

Fig. 7(a) shows the Raman spectrum of commercial TC powder before preparing TC antibiotic at varying concentrations on different substrates, obtained using a 785 nm excitation laser at RT. Notably, only the SERS data reveal distinct and well-resolved vibrational modes associated with TC. The Raman spectrum of TC on the SERS substrate exhibits a series of well-defined peaks at 661, 773, 995, 1215, 1275, 1334, 1436, and 1564 cm^{-1}, which align closely with the Raman spectrum of TC/Si(100). These vibrational modes become more distinct and are significantly enhanced on the SERS substrate. The Raman intensity of 10^4 ppm of TC/Si(100) is considerably weaker, ranging from 2.70 to 4.32 times and 1.33 to 2.10 times lower than those of 10 ppm and 100 ppm of $TC/Ag/SiO_2/Si(100)$ at the 661, 1215, 1275, 1334, and 1564 cm^{-1} bands. Additionally, slight shifts of approximately 2–8 cm^{-1} in the vibrational modes are observed compared to the pure TC powder. These shifts are likely due to the interaction between TC with water and the substrate surface. Despite these minor shifts, these modes remain consistent with the reference Raman spectrum of TC crystals [1–4,12,86,87], confirming the accuracy and reliability of the SERS substrate. This data suggests that the $Ag/SiO_2/Si(100)$ SERS substrate is highly sensitive and selective for TC detection, even at low concentrations.

Fig. 7(b) presents the SERS spectra of TC at various concentration levels on the Ag/SiO/Si(100) SERS substrate, compared to the pure TC powder on Si(100). The progressive enhancement of TC vibrational modes, particularly at 1215, 1275, and 1336 cm^{-1}, highlights the surface enhancement effects attributed to the Ag NPs. As the TC concentration decreases from 100 ppm to 0.01 ppm, the intensities of these peaks diminish by an EF value of approximately 5.8 to 3.4, respectively. Notably, the SERS intensity at the 1275 cm^{-1} peak significantly increases with the increase in TC concentration, indicating the high sensitivity of the $Ag/SiO_2/Si(100)$ substrate. Even at a low concentration of 0.1 ppm, the SERS spectrum still exhibits distinct peaks, with the 1275 cm^{-1} signal being approximately twice as intense as that at 0.01 ppm and about three times weaker than at 100 ppm. To elucidate the enhancement mechanism, coupling Ag NPs and SiO_2 NSs under 785 nm irradiation creates a substantial localized electric field driven by the resonance effect. This enhanced EM field, primarily at the Ag NP edges and tips, arises from localized SPR and is further amplified by the light-scattering properties of SiO_2 NSs. The morphology of Ag NPs and the interaction with SiO_2 significantly contribute to this field enhancement, enabling TC detection at sub-ppm levels. In addition, the scattering effect of SiO_2 NSs reflects and re-irradiates the Ag NPs, producing secondary field enhancements that intensify the overall SERS signal [2,59]. This effect, combined with the CT mechanism between the Ag/SiO_2 heterostructure NCs and the TC molecule, facilitates polarization of the TC, enlarging its Raman scattering cross-section. This CT is further supported by the matching energies of the Ag/SiO_2 plasmon modes and the highest occupied molecular orbital (HOMO) of TC, enhancing Raman signal intensities [2,89]. The role of SiO_2 also extends to molecular trapping, as it effectively captures TC molecules, concentrating them on the SERS substrate. This molecular enrichment and optical plasmon effects in the Ag NPs further contribute to signal enhancement due to optical attractive forces between Ag NPs and SiO_2 NSs under laser excitation. In addition, these effects synergistically boost the sensitivity of the $Ag/SiO_2/Si(100)$ substrate for the reliable detection of trace TC concentrations [90].

Fig. 8(a) presents the linear fitting plot of logarithmic TC concentration versus SERS intensity at the 1275 cm^{-1} peak. The plot demonstrates a robust linear correlation between the $logC_{TC}$ plot and Raman intensity at 1275 cm^{-1}, yielding a calibration equation of $I_{SERS} = 840.logC_{TC} + 1969$ with a correlation coefficient (R^2) of 0.968. The limit of detection (LOD) for TC was estimated to be approximately 0.01 ppm within a linear detection range of 0.01–100 ppm, as shown in Table 3. However, the R^2 value is slightly lower than in previous studies at similar TC concentrations [1–3,86]. This is likely due to the lack of optimization in parameters such as the size of the SiO_2 NS, Ag NPs, substrate, incident laser spot size, and absorption time of TC on the SERS substrate. Nevertheless, the results are more significant than those reported in other studies [12,71,76], affirming the efficacy of this system for detecting TC at sub-ppm concentrations.

The EF was calculated using Eq. (3) [3], which compares the SERS intensity of $TC/Ag/SiO_2/Si(100)$ substrate to the Raman intensity of TC/Si(100):

$$EF = \frac{I_{SERS}/C_{SERS}}{I_{Raman}/C_{Raman}}, \quad (3)$$

where I_{SERS} is the SERS intensity of $TC/Ag/SiO_2/Si(100)$, N_{SERS} is the number of SERS molecules, I_{Raman} is the Raman intensity of TC/Si(100),

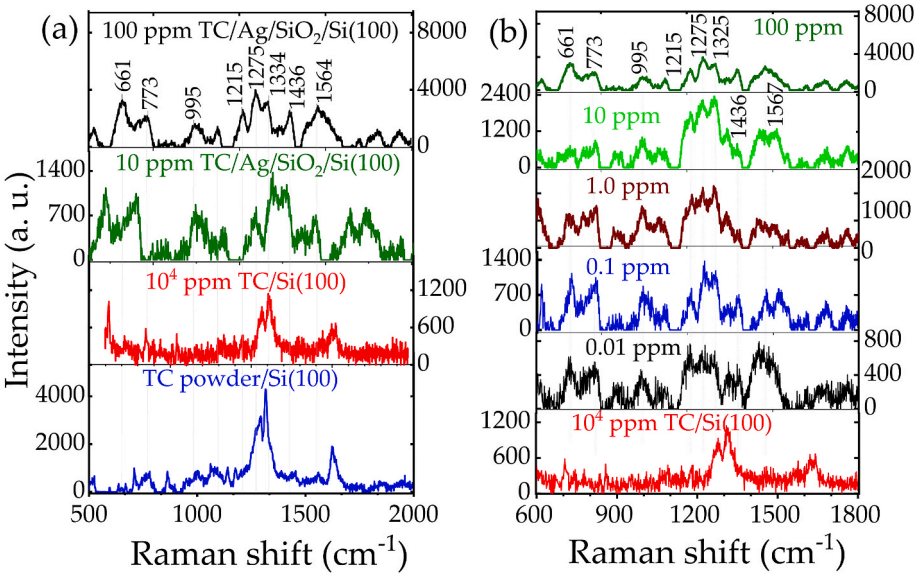

Fig. 7. (a) (Color online) SERS spectra of 100 and 10 ppm TC on the $Ag/SiO_2/Si(100)$ SERS substrate, compared with Raman spectra of 10^4 ppm TC and TC powder on the Si(100) substrate. (b) SERS spectra of TC with concentrations ranging from 0.01 to 100 ppm, measured on the $Ag/SiO_2/Si(100)$ SERS substrate, with an acquisition time of 30 s. (For interpretation of the references to color in this figure legend, the reader is referred to the Web version of this article.)

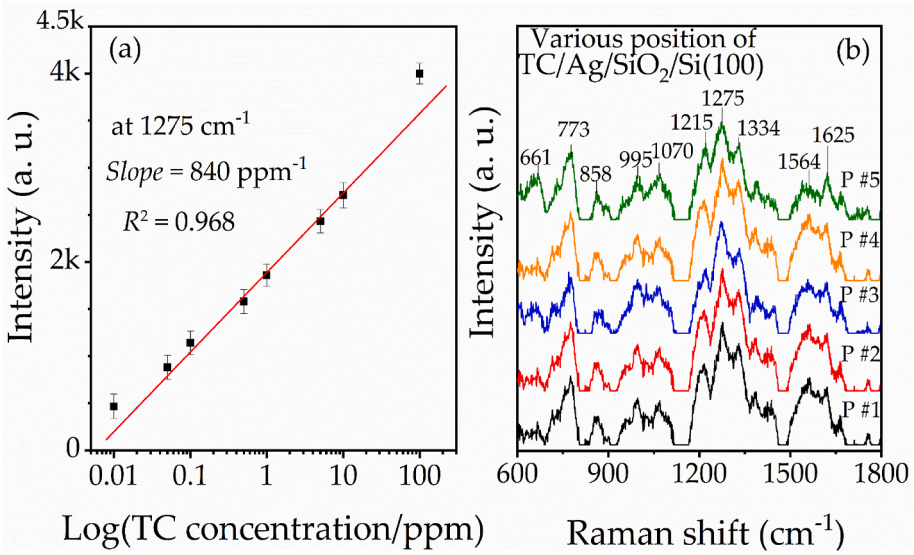

Fig. 8. (a) (Color online) Linear correlation between TC concentration in water and SERS intensity at 1275 cm^{-1} peak, (b) SERS spectra of 100 ppm TC concentration at different positions on the SERS substrate, with an acquisition time of 30 s. (For interpretation of the references to color in this figure legend, the reader is referred to the Web version of this article.)

Table 3
Enhancement factor (EF) on $Ag/SiO_2/Si(100)$ for various TC concentrations at 1275 cm^{-1} peak.

TC concentration (ppm)	Peak position (cm^{-1})	EF
100	1275	0.3×10^4
10	1275	1.7×10^4
5	1275	3.1×10^4
1.0	1275	1.5×10^5
0.5	1275	7.2×10^5
0.1	1275	1.2×10^6
0.05	1275	1.4×10^6
0.01	1275	4.6×10^6

and N_{Raman} is the number of molecules contributing to the Raman signal. The average EF at a TC concentration of 0.01 ppm was estimated to be approximately 4.6 x 10^6, 1-2 orders of magnitude higher than the EF values at TC concentrations ranging from 100 to 1.0 ppm (Table 3). This EF improvement is attributed to the combined effect of the EM field enhancement under the excitation of surface plasmon in Ag NP and the CT enhancement mechanism. The plasmon-enhanced electric fields surrounding the Ag NPs amplify the incident and scattered Raman fields up to 4 orders of magnitude [91]. Additionally, the efficient interface between Ag NPs and SiO_2 NSs heterojunction, as well as the interaction between Ag NPs and TC molecule, facilitate rapid CT process from HOMO to LUMO of TC under incident light. This CT process enhances the polarization of TC molecules, increasing the EF value [2,91].

The SERS data confirms the ability to detect sub-ppm levels of TC (as low as 0.01 ppm) with high sensitivity and stability. This detection sensitivity is lower than reported in other studies using Ag/SiO_2 NC-based SERS substrate, as summarized in Table 4, but remains satisfactory for practical applications. The uniform sensitivity of 100 ppm TC/$Ag/SiO_2/Si(100)$ was also validated by comparing SERS spectra obtained from five different points on the SERS substrate, as shown in Fig. 8(b). All spectra consistently exhibited vibrational bands in the 661–1625 cm^{-1} range, indicating uniform SERS performance across the substrate. The relative deviation is 8.4 % (well within the acceptable range of <10 %), demonstrating that the $Ag/SiO_2/Si(100)$ substrate provides reliable and reproducible SERS detection with high uniformity.

Table 4
Comparison of TC detection using different materials and methods.

Detection methods	Material structures	LOD (ppm)	Linear range (ppm)	Real samples	*Ref.*
Raman, SERS	Ag/SiO_2 NPs	0.01	0.01–100	Water	This work
Raman, SERS	Ag nano colloids	0.01	0.01–1000	Bovine milk	[6]
Raman, SERS	$Au/ND/C_3N_4$ hybrids	3.55×10^{-8}	0.03 — 3.55×10^{-8}	Water	[2]
Raman, SERS	Au nanostars	4.0×10^{-5}	0.005–0.05	Water	[1]
Raman, SERS	Ag nanoparticle arrays	3.55×10^{-5}	3.55×10^{-5} — 0.355	Milk, spiked water	[3]
Raman, SERS	Au/Ag nanoparticles	2.5×10^{-9}	2.5×10^{-9} — 0.01	Wastewater, serum	[9]
Fluorescence	$Tb(NO_3)_3.H_2O/H_2L$	6.4×10^{-3}	0–3.55	Raw milk	[14]
Fluorescence	AuCu nanocluster @ZIF8	1.7×10^{-4}	7.1×10^{-4} — 0.023	Raw milk	[43]
Fluorescence	Ag nanocluster and Er	3.73×10^{-4}	0—10.6×10^{-4}	Milk and honey	[17]
Fluorescence	Se-doped carbon dots	3.73×10^{-3}	1.7×10^{-3} —0.0142	Tap water	[19]
Fluorescence	W_xO_y quantum dots	6.75×10^{-4}	0–0.05	Milk powder	[18]
LRET, luminescence	MnO_2 nanosheets	8.5×10^{-6}	10^{-5} —0.1	Eggs, honey, milk, fish	[8]
Photoluminesce	Carbon dots	6.75×10^{-4}	3.55×10^{-4} — 1.42	Tap water, milk powder	[7]
HPLC, UV–Vis	–	5×10^{-4} — 1.0	–	Bovine milk, water, human plasma	[15]
EIS	$MBCPE/Fe_3O_4$ NP@OA	1.35×10^{-10}	3.55×10^{-10} —0.0355	Raw milk, blood serum, honey	[20]
DPV		1.1×10^{-8}	3.55×10^{-8} — 0.0355		
ELISA	Biotin—avidin	3.55×10^{-6}	1.12×10^{-5} — 0.0112	Milk	[21]

—non-investigation, NP—nanoparticle; LOD—limit of detection; ICA—immunochromatographic assay; LRET—luminescence resonance energy transfer; ELISA—enzyme-linked immune assy; DPV—differential pulse voltammetry; EIS—electrochemical impedance spectroscopy.

The spectra were also clearly discernible additional characteristic TC bands at 611, 773, 858, 995, 1070, 1215, 1334, 1564, and 1625 cm^{-1}. The relatively uniform and reproducible surface of the $Ag/SiO_2/Si(100)$ substrate, prepared by the coating method, meets the requirements for a robust and consistent SERS substrate [92,93], making it a promising candidate for sensitive TC detection in future applications.

4. Conclusions

In summary, an Ag/SiO_2-based SERS substrate was developed for the ultrasensitive detection of tetracycline in water samples. The Ag/SiO_2 NC, synthesized via the Stöber method coupled with chemical reduction, exhibited a well-defined architecture with uniformly distributed Ag NPs on SiO_2 NCs. The substrate achieved a remarkable enhancement factor (EF $\sim 10^6$) for tetracycline detection at sub-ppm levels (<1.0 ppm), attributed to efficient charge transfer, molecular enrichment, enhanced light scattering, and secondary plasmonic effect. Notably, the sensor demonstrated a detection limit as low as 0.01 ppm, with a strong linear correlation between tetracycline concentration and SERS intensity ($R^2 = 0.968$), underscoring its reliability for quantitative analysis. These findings suggest that the Ag/SiO_2 NC is a promising candidate for SERS-based chemical sensing, offering high sensitivity and selectivity for trace contaminant detection in environmental and pharmaceutical applications.

CRediT authorship contribution statement

Nguyen Thi Hue: Writing – original draft, Investigation, Funding acquisition, Formal analysis, Data curation, Conceptualization. **Tien Dai Nguyen:** Writing – review & editing, Writing – original draft, Resources, Methodology, Investigation, Conceptualization. **Hong Van Bui:** Writing – review & editing, Writing – original draft, Investigation, Formal analysis, Data curation, Conceptualization. **Thi Bich Vu:** Writing – original draft, Investigation, Data curation, Conceptualization. **Dang Van Thai:** Methodology, Investigation, Formal analysis. **Thuy Phuong Nhat Tran:** Writing – original draft, Formal analysis, Data curation. **Duc Tran Trong:** Investigation, Formal analysis, Data curation. **Huong Giang Nguyen Thi:** Data curation, Conceptualization. **Quoc Tran Ha:** Methodology, Formal analysis, Data curation. **Nguyen Manh Hung:** Writing – original draft, Investigation.

Declaration of competing interest

The authors declare that they have no conflict of interest and have not competed in this manuscript.

Acknowledgments

This research is funded by the fundamental research program of Hung Vuong University under project grant number N^o: 15/2022/HĐKH (HV15.2022)

Appendix A. Supplementary data

Supplementary data to this article can be found online at https://doi.org/10.1016/j.matchemphys.2025.130885.

Data availability

Data will be made available on request.

References

[1] J. Qian, C. Xing, Y. Ge, R. Li, A. Li, W. Yan, Gold nanostars-enhanced raman fingerprint strip for rapid detection of trace tetracycline in water samples, Spectroc. Acta Pt. A-Molec. Biomolec. Spectr. 232 (2020) 118146.
[2] J. Pei, Z. Tian, X. Yu, S. Zhang, S. Ma, Y. Sun, R. Boukherroub, Highly-sensitive SERS detection of tetracycline: sub-Enhancement brought by light scattering of nano-diamond, Appl. Surf. Sci. 608 (2023) 155270.
[3] M. Muhammad, B. Yan, G. Yao, K. Chao, C. Zhu, Q. Huang, Surface-enhanced raman spectroscopy for trace detection of tetracycline and dicyandiamide in milk using transparent substrate of Ag nanoparticle arrays, ACS Appl. Nano Mater. 3 (7) (2020) 7066–7075.
[4] M.A. Gab-Allah, Y.G. Lijalem, H. Yu, D.K. Lim, S. Ahn, K. Choi, B. Kim, Accurate determination of four tetracycline residues in chicken meat by isotope dilution-liquid chromatography/tandem mass spectrometry, J. Chromatogr. A (2023), 1691 463818.
[5] R. Parthasarathy, C.E. Monette, S. Bracero, S. Saha, M, Methods for field measurement of antibiotic concentrations: limitations and outlook, FEMS Microbiol. Ecol. 94 (8) (2018).
[6] S. Dhakal, K. Chao, Q. Huang, M. Kim, W. Schmidt, J. Qin, C.L. Broadhurst, A simple surface-enhanced raman spectroscopic method for on-site screening of tetracycline residue in whole milk, Sensors 18 (2) (2018) 424.
[7] N. Sharma, K. Yun, Dual sensing of tetracycline and l-Lysine using green synthesized carbon dots from Nigella sativa seeds, Dyes and Pigment. 182 (2020) 108640.
[8] R. Liu, S.A. Haruna, S. Ali, J. Xu, Q. Ouyang, H. Li, Q. Chen, An Up-conversion signal probe-MnO_2 nanosheet sensor for rapid and sensitive detection of tetracycline in food, Spectroc. Acta Pt. A-Molec. Biomolec. Spectr. 270 (2022) 120855.
[9] S. Liu, S. Li, S. Gao, High-throughput broad-spectrum analysis of tetracyclines via surface-enhanced raman spectroscopy imaging technology, Chem. Eng. J. 484 (2024) 149517.
[10] C.F. Leypold, M. Reiher, G. Brehm, M.O. Schmitt, S. Schneider, P. Matousek, M. Towrie, Tetracycline and Derivatives—Assignment of IR and Raman spectra via DFT calculations, Phys. Chem. Chem. Phys. 5 (6) (2003) 1149–1157.
[11] A. Khezerlou, M. Tavassoli, B. Khalilzadeh, A. Ehsani, H. Kazemian, Metal-organic framework-based advanced sensing platforms for the detection of tetracycline in food and water samples, Food Control (2023), 153 109965.
[12] S. Dhakal, K. Chao, Q. Huang, M. Kim, W. Schmidt, J. Qin, C.L. Broadhurst, A simple surface-enhanced raman spectroscopic method for on-Site screening of tetracycline residue in whole milk, Seensors 18 (2) (2018) 424.
[13] Codex alimentarius international food standars. https://www.fao.org/fao-who-codexalimentarius/sh-proxy/en/?lnk=1&url, 2023.
[14] X. Liu, Q. Ma, X. Feng, R. Li, X. Zhang, A recycled Tb-MOF fluorescent sensing material for highly sensitive and selective detection of tetracycline in milk, Microchem. J. 170 (2021) 106714.
[15] S. Shariati, Y. Yamini, A. Esrafili, Carrier mediated hollow fiber liquid phase microextraction combined with HPLC–UV for preconcentration and determination of some tetracycline antibiotics, J. Chromatogr. B 877 (4) (2009) 393–400.
[16] M.-R. Chao, C.-W. Hu, J.-L. Chen, Comparative syntheses of tetracycline-imprinted polymeric silicate and acrylate on CdTe quantum dots as fluorescent sensors, Biosens. Bioelectron. 61 (2014) 471–477.
[17] J. Xu, J. Wang, Y. Li, L. Zhang, N. Bi, J. Gou, T. Zhao, L. Jia, A wearable gloved sensor based on fluorescent Ag nanoparticles and europium complexes for visualized assessment of tetracycline in food samples, Food Chem. (2023), 424 136376.
[18] X. Wang, L. Li, H. Jiang, H. Zhangsun, Q. Wang, X. Sun, L. Wang, Highly selective and sensitive fluorescence detection of tetracyclines based on novel tungsten oxide quantum dots, Food Chem. 374 (2022) 131774.
[19] P. Chauhan, S. Chaudhary, One step production of Se doped carbon dots for rapid sensing of tetracycline in real water sample, Opt. Mater. 121 (2021) 111638.
[20] S. Jahanbani, A. Benvidi, Comparison of two fabricated aptasensors based on modified carbon paste/oleic acid and magnetic bar carbon paste/Fe_3O_4@oleic acid nanoparticle electrodes for tetracycline detection, Biosens. Bioelectron. 85 (2016) 553–562.
[21] M. Jeon, J. Kim, K.-J. Paeng, S.-W. Park, I.R. Paeng, Biotin–avidin mediated competitive enzyme-linked immunosorbent assay to detect residues of tetracyclines in milk, Microchem. J. 88 (1) (2008) 26–31.
[22] H. Tajik, H. Malekinejad, S.M. Razavi-Rouhani, M.R. Pajouhi, R. Mahmoudi, A. Haghnazari, Chloramphenicol residues in chicken liver, kidney and muscle: a comparison among the antibacterial residues monitoring methods of four plate test, ELISA and HPLC, Food Chem. Toxicol. 48 (8) (2010) 2464–2468.
[23] I. Ali, Y, A.-E.H, G.V. K, S. Prashant, U. Negi, Analyses of chloramphenicol in biological samples by HPLC, Anal. Lett. 42 (10) (2009) 1368–1381.
[24] M. Jing, H. Zhang, M. Li, Z. Mao, X. Shi, Silver nanoparticle-decorated TiO_2 nanotube array for solid-phase microextraction and SERS detection of antibiotic residue in milk, Spectroc. Acta Pt. A-Molec. Biomolec. Spectr. (2021), 255 119652.
[25] M. Girmatsion, A. Mahmud, B. Abraha, Y. Xie, Y. Cheng, H. Yu, W. Yao, Y. Guo, H. Qian, Rapid detection of antibiotic residues in animal products using surface-enhanced raman spectroscopy: a review, Food Control 126 (2021) 108019.
[26] C. Karthik, D.G. Caroline, M. Dhanam Priya, Pandi Prabha, S. Synthesis, Characterization of Ag-SiO_2 nanocomposite and its application in food packaging, J. Inorg. Organomet. Polym. Mater. 31 (6) (2021) 2532–2541.
[27] Y. Zhang, Y. Huang, Y. Kang, J. Miao, K. Lai, Selective recognition and determination of malachite green in fish muscles via surface-enhanced raman scattering coupled with molecularly imprinted polymers, Food Control (2021), 130 108367.
[28] Y. Zhang, L. Li, Y. Gao, X. Wang, L. Sun, W. Ji, Y. Ozaki, Nitrosonaphthol reaction-assisted SERS assay for selective determination of 5-hydroxyindole-3-acetic acid in human urine, Anal. Chim. Acta (2020) 34–40.

[29] S.M. Restaino, I.M. White, A critical review of flexible and porous SERS sensors for analytical chemistry at the point-of-sample, Anal. Chim. Acta (2019) 17–29.
[30] D. Sun, W. Xu, C. Liang, W. Shi, S. Xu, Smart surface-enhanced resonance raman scattering nanoprobe for monitoring cellular alkaline phosphatase activity during osteogenic differentiation, ACS Sens. 5 (6) (2020) 1758–1767.
[31] M. Assis, L.G.P. Simoes, G.C. Tremiliosi, L.K. Ribeiro, D. Coelho, D.T. Minozzi, R. I. Santos, D.C.B. Vilela, L.H. Mascaro, J. Andrés, E. Longo, PVC-SiO_2-Ag composite as a powerful biocide and anti-SARS-CoV-2 material, J. Polym. Res. 28 (9) (2021) 361.
[32] M. Assis, L.G.P. Simoes, G.C. Tremiliosi, D. Coelho, D.T. Minozzi, R.I. Santos, D.C. B. Vilela, J.R.d. Santos, L.K. Ribeiro, I.L.V. Rosa, L.H. Mascaro, J. Andrés, E. Longo, SiO_2-Ag composite as a highly virucidal material: a roadmap that rapidly eliminates SARS-CoV-2, Nanomaterials 11 (3) (2021) 638.
[33] C.V. Khedkar, K.D. Daware, P.S. Badgujar, Y.D. Kolekar, S.W. Gosavi, S.I. Patil, Ag–SiO_2 nanocomposite for the optical detection of Hg(II) ions and catalytic reduction of methylene blue, Opt. Mater. 120 (2021) 111426.
[34] J. Alimunnisa, K. Ravichandran, K.S. Meena, Synthesis and characterization of Ag@SiO_2 core-shell nanoparticles for antibacterial and environmental applications, Mol. Liq. 231 (2017) 281–287.
[35] E. Al-Bermany, A.T.m. Mekhalif, H.A. Banimuslem, K. Abdali, M.M. Sabri, Effect of green synthesis bimetallic Ag@SiO_2 core–shell nanoparticles on absorption behavior and electrical properties of PVA-PEO nanocomposites for optoelectronic applications, Silicon 15 (9) (2023) 4095–4107.
[36] Z. Yin, F. Yuan, M. Xue, Y. Xue, Y. Xie, J. Ou, Y. Luo, Z. Hong, C. Xie, A multifunctional and environmentally safe superhydrophobic membrane with superior oil/water separation, photocatalytic degradation and anti-biofouling performance, J. Colloid Interface Sci. 611 (2022) 93–104.
[37] D.V. Thai, V.B. Pham, C.D. Sai, T.H.G. Nguyen, T.D. Tran, T.H. Tran, T.-T. Nguyen, T.D. Nguyen, H.V. Bui, Synthesis of SiO_2@Ag nanocomposite for investigating metal-enhanced fluorescence and surface-enhanced raman spectroscopy, J. Fluoresc. 34 (4) (2024) 1–10.
[38] Y. Guo, H. Lu, X. Jian, SiO_2–modified APTMS nanocoatings encapsulating FeNi: amplifying microwave absorption and corrosion resistance, Appl. Surf. Sci. 652 (2024) 159286.
[39] X.X. Han, R.S. Rodriguez, C.L. Haynes, Y. Ozaki, B. Zhao, Surface-enhanced raman spectroscopy, Nat. Rev. Methods Prim. 1 (1) (2022) 87.
[40] K.S. Alrashdi, A.M. Munshi, S.H. Alrefaee, A.I. Alalawy, H.M. Abumelha, W. M. Alamoudi, N.M. El-Metwaly, Miniaturization of palladium and gold in nanosize to hold immense potentiality for application in wool functional finishing, Fibers Polym. 25 (7) (2024) 2555–2568.
[41] M. Fahim, A. Shahzaib, N. Nishat, A. Jahan, T.A. Bhat, A. Inam, Green synthesis of silver nanoparticles: a comprehensive review of methods, influencing factors, and applications, JCIS Open 16 (2024) 100125.
[42] J. Jiang, Q. Shen, P. Xue, H. Qi, Y. Wu, Y. Teng, Y. Zhang, Y. Liu, X. Zhao, X. Liu, A highly sensitive and stable SERS sensor for malachite green detection based on Ag nanoparticles in situ generated on 3D MoS_2 nanoflowers, ChemistrySelect 5 (1) (2020) 354–359.
[43] S. Pan, Y. Zhu, G. Shi, Z. Shang, M. Wang, Synthesis of SiO_2 coated Ag-cicada wing as large scale surface enhanced fluorescence substrate, Optik 223 (2020) 165377.
[44] J. Huang, Y.-f. Zhou, J. Xu, P. Liang, Z.-g. Liu, J. Wang, D. Zhang, Q.-m. Dong, W.-m. Shen, S.-l. Zhuang, Unveiling the growth mechanism of SiO_2/Ag hybrid nanospheres and using for surface enhanced raman scattering detection, Appl. Surf. Sci. 463 (2019) 115–120.
[45] T. Taib, M.R. Johan, W.J. Basirun, Plasmonic SERS active nanostructured Ag–SiO_2 at optimum volume ratio synthesized via sol-gel technique, Physica B 606 (2021) 412638.
[46] P. Kumar, R. Khosla, M. Soni, D. Deva, S.K. Sharma, A highly sensitive, flexible SERS sensor for malachite green detection based on Ag decorated microstructured PDMS substrate fabricated from taro leaf as template, Sens. Actuator B-Chem. 246 (2017) 477–486.
[47] J. Zhao, C. Zhang, Y. Lu, Q. Wu, Y. Yuan, M. Xu, J. Yao, Surface-enhanced raman spectroscopic investigation on surface plasmon resonance and electrochemical catalysis on surface coupling reaction of pyridine at Au/TiO_2 junction electrodes, J. Raman Spectrosc. 51 (11) (2020) 2199–2207.
[48] L. Chen, F. Zhang, X.-Y. Deng, X. Xue, L. Wang, Y. Sun, J.-D. Feng, Y. Zhang, Y. Wang, Y.M. Jung, SERS study of surface plasmon resonance induced carrier movement in Au@Cu_2O core-shell nanoparticles, Spectrochim. Acta Part A Mol. Biomol. Spectrosc. 189 (2018) 608–612.
[49] A. Khataee, R. Jalili, M. Dastborhan, A. Karimi, A. Ebadi Fard Azar, Ratiometric visual detection of tetracycline residues in milk by framework-enhanced fluorescence of gold and copper nanoclusters, Spectroc. Acta Pt. A-Molec. Biomolec. Spectr. (2020), 242 118715.
[50] Z.G. Wu, Y.R. Jia, J. Wang, Y. Guo, J.F. Gao, Core-shell SiO_2/Ag composite spheres: synthesis, characterization and photocatalytic properties, Mater. Sci. 34 (4) (2016) 806–810.
[51] P.G. Etchegoin, E.C. Le Ru, A perspective on single molecule SERS: current status and future challenges, Phys. Chem. Chem. Phys. 10 (40) (2008) 6079–6089.
[52] E.C. Cheshari, X. Ren, X. Li, Core–shell Ag-molecularly imprinted composite for SERS detection of carbendazim, Int. J. Environ. Anal. Chem. 100 (11) (2020) 1245–1258.
[53] J. Junaidi, W. Sulistiani, Y. Efridahniar, I. Pratiwi, I. Firdaus, P. Manurung, P. Karo Karo, Synthesis and characterization of Ag/SiO_2 nanocomposite based on rice husk silica using sol-gel method, J. Nano Res. 78 (2023) 31–42.
[54] X. Feng, H. Li, Q. Zhang, P. Zhang, X. Song, J. Liu, L. Zhao, L. Gao, SiO_2–Ag–SiO_2 core/shell structure with a high density of Ag nanoparticles for CO oxidation catalysis, Nanotechnology 27 (45) (2016) 455605.
[55] B. Mahltig, E. Gutmann, M. Reibold, D.C. Meyer, H. Böttcher, Synthesis of Ag and Ag/SiO_2 sols by solvothermal method and their bactericidal activity, J. Sol. Gel Sci. Technol. 51 (2) (2009) 204–214.
[56] A. Abdal-hay, A.S. Hamdy, G.T. Abdel-Jaber, N.A.M. Barakat, A.A. Ebnalwaled, K. A. Khalil, A facile manufacturing of Ag/SiO_2 nanofibers and nanoparticles composites via a simple hydrothermal plasma method, Ceram. Int. 41 (9) (2015) 12447–12452. Part B.
[57] R. Zapata, M. Balestrieri, I. Gozhyk, H. Montigaud, R. Lazzari, On the O_2 "surfactant" effect during Ag/SiO_2 magnetron sputtering deposition: the point of view of in situ and real-time measurements, ACS Appl. Mater. Interfaces 15 (30) (2023) 36951–36965.
[58] P. Cheng, M. Ziegler, V. Ripka, D. Wang, H. Wang, P.A. van Aken, P. Schaaf, Bio-inspired self-assembly of large area 3D Ag@SiO_2 plasmonic nanostructures with tunable broadband light harvesting, Appl. Mater. Today 25 (2021) 101238.
[59] P. Karthick Kannan, P. Shankar, C. Blackman, C.-H. Chung, Recent advances in 2D inorganic nanomaterials for SERS sensing, Adv. Mater. 31 (34) (2019) 1803432.
[60] W. Stöber, A. Fink, E. Bohn, Controlled growth of monodisperse silica spheres in the micron size range, J. Colloid Interface Sci. 26 (1) (1968) 62–69.
[61] I.A. Rahman, P. Vejayakumaran, C.S. Sipaut, J. Ismail, C.K. Chee, Size-dependent physicochemical and optical properties of silica nanoparticles, Mater. Chem. Phys. 114 (1) (2009) 328–332.
[62] M.H. Ali, M.A.K. Azad, K.A. Khan, M.O. Rahman, U. Chakma, A. Kumer, Analysis of crystallographic structures and properties of silver nanoparticles synthesized using PKL extract and nanoscale characterization techniques, ACS Omega 8 (31) (2023) 28133–28142.
[63] H. Liu, J. Bai, S. Wang, C. Li, L. Guo, H. Liang, T. Xu, W. Sun, H. Li, The preparation of silver nanoparticles/carbon nanofibers as catalyst in the styrene epoxidation, Colloids Surf., A 448 (2014) 154–159.
[64] Y. Li, B.-P. Zhang, C.-H. Zhao, J.-X. Zhao, Structure transition, formation, and optical absorption property study of Ag/SiO_2 nanofilm by sol-gel method, J. Mater. Res. 27 (24) (2012) 3141–3146.
[65] C. Xu, W.-j. Li, Y.-m. Wei, X.-y. Cui, Characterization of SiO_2/Ag composite particles synthesized by in situ reduction and its application in electrically conductive adhesives, Mater. Des. 83 (2015) 745–752.
[66] T. Varadavenkatesan, S. Pai, R. Vinayagam, R. Selvaraj, Characterization of silver nano-spheres synthesized using the extract of Arachis hypogaea nuts and their catalytic potential to degrade dyes, Mater. Chem. Phys. 272 (2021) 125017.
[67] R.S. Dubey, Y.B.R.D. Rajesh, M.A. More, Synthesis and characterization of SiO_2 nanoparticles via sol-gel method for industrial applications, Mater. Today Proc. 2 (4) (2015) 3575–3579.
[68] T.N. Tran, T.V. Anh Pham, M.L. Phung Le, T.P. Thoa Nguyen, V.M. Tran, Synthesis of amorphous silica and sulfonic acid functionalized silica used as reinforced phase for polymer electrolyte membrane, Adv. Nat. Sci. Nanosci. Nanotechnol. 4 (4) (2013) 045007.
[69] Y. Liang, J. Ouyang, H. Wang, W. Wang, P. Chui, K. Sun, Synthesis and characterization of core–shell structured SiO_2@YVO_4:Yb^{3+},Er^{3+} microspheres, Appl. Surf. Sci. 258 (8) (2012) 3689–3694.
[70] D. Aguilar-García, A. Ochoa-Terán, F. Paraguay-Delgado, M.E. Díaz-García, G. Pina-Luis, Water-compatible core–shell Ag@SiO_2 molecularly imprinted particles for the controlled release of tetracycline, J. Mater. Sci. 51 (12) (2016) 5651–5663.
[71] E. Adamska, K. Niska, A. Wcisło, B. Grobelna, Characterization and cytotoxicity comparison of Silver- and silica-based nanostructures, Materials 14 (17) (2021) 4987.
[72] D. Niznansky, J.L. Rehspringer, Infrared study of SiO_2 sol to gel evolution and gel aging, J. Non-Cryst. Solids 180 (2) (1995) 191–196.
[73] D. Steinigeweg, S. Schlücker, Monodispersity and size control in the synthesis of 20–100 nm quasi-spherical silver nanoparticles by citrate and ascorbic acid reduction in glycerol–water mixtures, Chem. Commun. 48 (69) (2012) 8682–8684.
[74] Y.H. Kim, D.K. Lee, Y.S. Kang, Synthesis and characterization of Ag and Ag–SiO_2 nanoparticles, Colloids Surf., A (2005), 257-258 273-276.
[75] C. Wang, J.-J. Jian, Degradation and detoxicity of tetracycline by an enhanced sonolysis, J. Water Environ. Technol. 13 (4) (2015) 325–334.
[76] C. Wang, J. Jian, Feasibility of tetracycline wastewater degradation by enhanced sonolysis, J. Adv. Oxid. Technol. 18 (1) (2015) 39–46.
[77] J. Kang, H. Liu, Y.-M. Zheng, J. Qu, J.P. Chen, Application of nuclear magnetic resonance spectroscopy, fourier transform infrared spectroscopy, UV–Visible spectroscopy and kinetic modeling for elucidation of adsorption chemistry in uptake of tetracycline by zeolite beta, J. Colloid Interface Sci. 354 (1) (2011) 261–267.
[78] J.R.D. McCormick, S.M. Fox, L.L. Smith, B.A. Bitler, J. Reichenthal, V.E. Origoni, W.H. Muller, R. Winterbottom, A.P. Doerschuk, Studies of the reversible epimerization occurring in the tetracycline family. The preparation, properties and proof of structure of some 4-epi-Tetracyclines, J. Am. Chem. Soc. 79 (11) (1957) 2849–2858.
[79] Y. Zhao, Y. Tian, P. Ma, A. Yu, H. Zhang, Y. Chen, Determination of melamine and malachite green by surface-enhanced raman scattering spectroscopy using starch-coated silver nanoparticles as substrates, Anal. Methods 7 (19) (2015) 8116–8122.
[80] X. Wang, Y. Wang, D. Li, Degradation of tetracycline in water by ultrasonic irradiation, Water Sci. Technol. 67 (4) (2013) 715–721.
[81] J.U. Kiran, J.P. Roners, S. Mathew, XPS and thermal studies of silver doped SiO_2 matrices for plasmonic applications, Mater. Today Proc. 33 (2020) 1263–1267.
[82] Y.H. Kim, D.K. Lee, H.G. Cha, C.W. Kim, Y.S. Kang, Synthesis and characterization of antibacterial Ag−SiO_2 nanocomposite, J. Phys. Chem. C 111 (9) (2007) 3629–3635.

[83] F. Wang, D. Du, S. Liu, L. Wang, T. Jiao, Z. Xu, H. Wang, Revealing the hemispherical shielding effect of SiO_2@Ag composite nanospheres to improve the surface enhanced raman scattering performance, Nanomaterials 11 (9) (2021) 2209.
[84] G. Greczynski, L. Hultman, X-ray photoelectron spectroscopy: towards reliable binding energy referencing, Prog. Mater. Sci. 107 (2020) 100591.
[85] J.A. Jiménez, H. Liu, E. Fachini, X-ray photoelectron spectroscopy of silver nanoparticles in phosphate glass, Mater. Lett. 64 (19) (2010) 2046–2048.
[86] X. Chen, W. Liang, C. Yang, W. Lin, M. Bi, M.S. Proceedings, Simultaneous Quantitative Detection of Tetracyclines Derivatives by Raman Spectroscopy, IEE Xplore, 2012, pp. 111–114.
[87] J. Zhao, P. Liu, H. Yuan, Y. Peng, Q. Hong, M. Liu, Rapid detection of tetracycline residues in duck meat using surface enhanced raman spectroscopy, J. Spectro. 2016 (1) (2016) 1845237.
[88] M. Smirnov, E. Roginskii, A. Savin, A. Oreshonkov, D. Pankin, Density-functional study of the Si/SiO_2 interfaces in short-period superlattices: vibrational states and raman spectra, Photonics 10 (8) (2023) 902.
[89] H. Lai, H. Zhang, G. Li, Y.-f. Hu, Bimetallic AgNPs@dopamine modified-halloysite nanotubes-AuNPs for adenine determination using surface-enhanced raman scattering, Microchim. Acta 188 (4) (2021) 127.
[90] A.J. Hallock, P.L. Redmond, L.E. Brus, Optical forces between metallic particles, Proc. Natl. Acad. Sci. USA 102 (5) (2005) 1280–1284.
[91] K. Willets, K. Mayer, 16 - surface-enhanced raman scattering (SERS) as a characterization method for metal-organic interactions, in: O. Ostroverkhova (Ed.), Handbook of Organic Materials for Electronic and Photonic Devices, second ed., Woodhead Publishing, 2019, pp. 529–549.
[92] Y. Luo, B. Zhai, M. Li, W. Zhou, J. Yang, Y. Shu, Y. Fang, Self-adhesive, surface adaptive, regenerable SERS substrates for in-situ detection of urea on bio-surfaces, J. Colloid Interface Sci. 660 (2024) 513–521.
[93] L. Wu, W. Wang, W. Zhang, H. Su, Q. Liu, J. Gu, T. Deng, D. Zhang, Highly sensitive, reproducible and uniform SERS substrates with a high density of three-dimensionally distributed hotspots: gyroid-structured Au periodic metallic materials, NPG Asia Mater. 10 (1) (2018) e462-e462.